



Three-dimensional electroconvective vortices in cross flowYifei Guan ^{1,*}, James Riley,¹ and Igor Novosselov ^{1,2}¹*Department of Mechanical Engineering, University of Washington, Seattle, Washington 98195, USA*²*Institute for Nano-Engineered Systems, University of Washington, Seattle, Washington 98195, USA*

(Received 11 August 2019; accepted 5 February 2020; published 3 March 2020)

This study focuses on the three-dimensional (3D) electrohydrodynamic flow instability between two parallel electrodes driven by unipolar charge injection with and without cross flow. Lattice Boltzmann method with a two-relaxation time model is used to compute flow patterns. In the absence of cross flow, the base-state solution is hydrostatic, and the electric field is one-dimensional. With strong charge injection and high electrical Rayleigh number, the system exhibits electroconvective vortices. Disturbed by perturbation patterns, such as rolling pattern, square pattern, and hexagon pattern, the flow develops corresponding to the most unstable mode. The growth rate and pattern transitions are studied using dynamic mode decomposition of the transient numerical solutions. The interactions between cross flow and electroconvective vortices lead to suppression and disappearance of structures with velocity components in the direction of cross flow, while the other components are not affected. Surprisingly, the transition from a 3D to a 2D flow pattern enhances the convective charge transport, marked by an increase in the electric Nusselt number. Hysteresis in the 3D to 2D transition is characterized by the nondimensional parameter Y , a ratio of the electrical force term to the viscous term in the momentum equation.

DOI: [10.1103/PhysRevE.101.033103](https://doi.org/10.1103/PhysRevE.101.033103)**I. INTRODUCTION**

Both two-dimensional (2D) and three-dimensional (3D) vortex structures are ubiquitous in fluid systems. In considering convection, various flow patterns have been observed as a result of body forces acting on the fluid, e.g., Rayleigh-Benard convection (RBC) [1–7], Marangoni effects [8–12], magnetoconvection [13–18], and magnetohydrodynamics convection [19–26]. The electrical force on the fluid is known as electroconvection (EC) such as electrokinetics instability (EKI) [27–31] and electrohydrodynamic (EHD) convection [32–35]. EC phenomenon has been first reported by G. I. Taylor in 1966 describing cellular convection in a liquid droplet [36]. Since then, EC has been observed in other systems with the interaction of electrical forces with fluids. In nonequilibrium EHD systems [7,34–52], poorly conductive leaky dielectric fluid acquires unipolar charge injection at the interface in response to the electric field. In charge-neutral electrokinetic (EK) systems, electroconvection is triggered by the electroosmotic slip of the electrolyte in the electric double layer at membrane surfaces [27,28,31,53–59].

The EC stability problem was first analyzed by a reduced nonlinear hydraulic model [60,61] and by a linear stability analysis without the charge diffusion term [62,63]. Atten and Moreau [64] showed that, in the weak-injection limit, $C \ll 1$, the flow stability is determined by the parameter $T_c C^2$, where C is the charge injection level and T_c is the linear stability threshold for the electrical Rayleigh number T , the ratio of the electrical force to the viscous force [Eq. (9)]. In the space-charge-limited (SCL) injection ($C \rightarrow \infty$), the flow stability

depends on T_c alone [65–67]. The effect of charge diffusion was investigated by Zhang *et al.* using linear stability analysis [47] and nonlinear analysis [51]. The authors found that the charge diffusion has a nonnegligible effect on T_c .

EC patterns have also been observed in liquid crystals when induced by an alternating current (AC). Dennin *et al.* have shown the evolution of spatiotemporal chaos (STC) in nematic liquid crystals can be described by supercritical Hopf bifurcation [33]. Dennin *et al.* reported that the inclusion of the dissociation-recombination reaction of the ionic dopant in the EC model predicts STC behavior [32]. Daya *et al.* reported the bifurcations in annular EC in a weakly conducting smectic liquid crystal film between rotating cylinders [40,68,69]. John *et al.* demonstrated that the EC flow field could lead to 3D EC structures based on the perturbation patterns (rolling, triangular, and square patterns) [70]. Buka *et al.* showed other patterns that depend on the anisotropy of EC [71]. More recently, Huh reported noise-induced traveling waves (moving rolls) with AC-driven EC in a nematic liquid crystal [72] and noise-free EC in one-dimensional liquid crystal cells [73].

In the presence of shear flow, the parameterization of EC stability is somewhat analogous to Rayleigh-Benard convection (RBC) [74–82]. Mohamad *et al.* used a nondimensional group Gr/Re^2 , the ratio of the buoyancy to the inertia force, to parametrize the effect of applied shear, where Gr is the Grashof number [75]. For $Gr/Re^2 > 10$, the impact of the cross flow is insignificant, while for $Gr/Re^2 < 0.1$, the effect of buoyancy can be neglected. Reduced nonlinear models such as Ginzburg-Landau equations are used to study the transitional behavior of RBC cells [74,76–78].

For the EC problem, Daya *et al.* showed that the primary bifurcation of 2D annular EC with rotating cylinders (Couette cross flow) could be switched between supercritical and

*gyf135@uw.edu

subcritical by changing radius ratio and Re [40]. They showed that the onset of an annular EC is via a supercritical bifurcation, but a sufficiently large shear can change the bifurcation from supercritical to subcritical [68]. The authors also showed that the Couette cross flow suppresses the onset of annular EC [69]. Kwak *et al.* have examined the effect of the cross flow on the EKI and proposed a scaling law relating the field strength and shear to the height of the EC vortices [56]. Later, Kwak *et al.* extended the scaling law analysis for the electric Nusselt number as a function of the electric Rayleigh and Reynolds numbers for the EC-induced convective ion transport [83]. Magnico reported the numerical results for EKI near an ion exchange membrane with the pressure-driven shear flow and showed that the spatial distribution of forces controls the dynamics of vortex association and dissociation [84]. Linear stability analysis of the 2D EHD-EC with cross flow was reported by Zhang *et al.* [47], and nonlinear analysis was reported more recently [51]. Zhang *et al.* found that and the transient behavior depends on the Reynolds number. Li *et al.* performed linear analysis for convective instabilities in EHD-Poiseuille flow and found that the ratio of the Coulomb force to the viscous force affects the transition of transverse rolls from convective to absolute instability [85]. Traore *et al.* showed that, in 2D finite-volume simulations of Poiseuille flow, the value of T_c is a function of Re and the ion mobility parameter, M [48]. More recently, Traore *et al.* investigated the EHD-EC behavior between two rotating coaxial cylinders via a finite-volume method and showed that the shear motion increases the stability of the flow system [86]. Guan and Novosselov used 2D numerical simulations to parameterize the decay of EC vortex pairs to the base cross flow in terms of a nondimensional ratio of electrical to viscous forces, Y [87].

The transition from 3D to 2D structures under the influence of ambient shear has been studied in the formation of atmospheric cloud streets in planetary boundary layers [88–90], and in laboratory RBC studies [74–78]. In EC systems the interaction of the forcing term is different from RBC; however, 3D vortex pattern transition has been observed. Pham *et al.* presented a numerical and experimental study of the 3D effect in EKI. The shear flow stretched the 3D vortex patterns streamwise forming helical flow patterns [91]. However, the mechanism and the detailed analysis of the transition in EC systems have not been presented. The nonlinear effects and the flow transition in the shear flow with 3D EHD-EC vortices have not been analyzed, partially due to the lack of 3D data.

Numerical simulation can shed insight into the behavior of EC vortices. Early work has shown that in finite-difference modeling, strong numerical diffusivity can lead to ambiguity in the prediction of stability criteria [39]. Other numerical approaches have been developed, including the particle-in-cell method [92], the finite-volume method with flux-corrected transport [93] or the total variation diminishing scheme [43,45,49,50,94], and the method of characteristics [95]. Luo *et al.* showed that a unified Lattice Boltzmann model (LBM) predicts the linear and finite-amplitude stability criteria of the subcritical bifurcation in the EC flow for both 2D and 3D flow scenarios [7,34,35,52,96]. A segregated solver was proposed that combines a two-relaxation time (TRT) LBM modeling of the fluid and charge transport, and a Fast Fourier Transform (FFT) Poisson solver for the electrical field [97].

Analysis of the complex flow structures has been studied by multiple researchers, and currently, several tools are available. Among other methods, dynamic mode decomposition (DMD) has been used. DMD analysis can be performed on experimental measurements or numerical solutions to gain insight into the spatiotemporal dynamics of complex systems [98]. Schmid and colleagues first applied DMD to stability analysis of fluid flow [99,100]. The eigenmodes from DMD are equivalent to global modes if the linearized equations are used in numerical simulations. DMD has also been used to identify bifurcation points in complex systems such as flow in a lid-driven cavity at high Reynolds number [101], to reconstruct compressed high-dimensional data of a fluid system [102], and to extract coherent spatiotemporal structures in fluid flows for prediction and control [103,104]. The use of DMD for EC flow and flow pattern transition analysis, however, has not been previously reported.

This work investigates the behavior of 3D EHD-EC flow patterns in cross flow with unipolar charge injection. Couette and Poiseuille cross flows are added to EC convection to trigger flow transition. The vortex structure evolution is analyzed by DMD. The effects of cross flow are parameterized by a nondimensional number, Y , a ratio of electrical to viscous forces in the dimensionless Navier-Stokes equations.

II. GOVERNING EQUATIONS AND DIMENSIONAL ANALYSIS

The governing equations for the system are the Navier-Stokes equations (NSE) with an electrical forcing term $\mathbf{F}_e = -\rho_c \nabla \varphi$ added to the momentum equation, the charge transport equation, and the Poisson equation for the electrical potential.

$$\nabla \cdot \mathbf{u} = 0, \quad (1)$$

$$\rho \frac{D\mathbf{u}}{Dt} = -\nabla P + \mu \nabla^2 \mathbf{u} - \rho_c \nabla \varphi, \quad (2)$$

$$\frac{\partial \rho_c}{\partial t} + \nabla \cdot [(\mathbf{u} - \mu_b \nabla \varphi) \rho_c - D_c \nabla \rho_c] = 0, \quad (3)$$

$$\nabla^2 \varphi = -\frac{\rho_c}{\varepsilon}, \quad (4)$$

where ρ and μ are the density and the dynamic viscosity of the working fluid, $\mathbf{u} = (u_x, u_y, u_z)$ is the velocity vector field, P is the static pressure, ρ_c is the charge density, μ_b is the ion mobility, D_c is the ion diffusivity, ε is the electrical permittivity, and φ is the electrical potential. The electrical force is a source term in the momentum equation [Eq. (2)] [47,105–107]. The variables to be solved are the velocity field \mathbf{u} , pressure P , charge density ρ_c , and electrical potential φ . The flow is assumed to be periodic in the x and y directions, and wall-bounded z direction. Cross flow is applied in the x direction.

In the absence of cross flow, the system can be nondimensionalized with the characteristics of the electric field [47]: H is the distance between the electrodes (two plates infinite in x and y), ρ_0 is the injected charge density at the anode, and $\Delta\varphi_0$ is the voltage difference applied to the electrodes. The time t is nondimensionalized by $H^2/(\mu_b \Delta\varphi_0)$, the velocity

\mathbf{u} by the drift velocity of the ions $u_{\text{drift}} = \mu_b \Delta \varphi_0 / H$, the pressure P by $\rho_0 (\mu_b \Delta \varphi_0)^2 / H^2$, and the charge density ρ_c by ρ_0 . Therefore, the nondimensionalization of the governing equations [Eqs. (1)–(4)] gives

$$\nabla^* \cdot \mathbf{u}^* = 0, \quad (5)$$

$$\frac{D^* \mathbf{u}^*}{D^* t^*} = -\nabla^* P^* + \frac{M^2}{T} \nabla^{*2} \mathbf{u}^* - CM^2 \rho_c^* \nabla^* \varphi^*, \quad (6)$$

$$\frac{\partial^* \rho_c^*}{\partial^* t^*} + \nabla^* \cdot \left[(\mathbf{u}^* - \nabla^* \varphi^*) \rho_c^* - \frac{1}{F_e} \nabla^* \rho_c^* \right] = 0, \quad (7)$$

$$\nabla^{*2} \varphi^* = -C \rho_c^*, \quad (8)$$

where the asterisk denotes nondimensional variables. These nondimensional equations yield four dimensionless parameters describing the system's state [7,34,35,43–52,94]:

$$M = \frac{(\varepsilon/\rho)^{1/2}}{\mu_b}, \quad T = \frac{\varepsilon \Delta \varphi_0}{\mu \mu_b}, \quad C = \frac{\rho_0 H^2}{\varepsilon \Delta \varphi_0}, \quad F_e = \frac{\mu_b \Delta \varphi_0}{D_e}. \quad (9)$$

The physical interpretations of these four nondimensional parameters are as follows: M is the mobility ratio between hydrodynamic mobility and the ionic mobility, T is the electrical Rayleigh number, a ratio between the electrical force and the viscous force, C is the strength of injection [47,51], and F_e is the reciprocal charge diffusivity coefficient [47,51,85].

With the addition of a cross flow, the velocity term in the nondimensional momentum equation is modified to account for the external flow, \mathbf{u}_{ext} , which is different from the previous formulation where the drift charge velocity was used [87]. Here we use the velocity of the upper wall in Couette flow or the centerline velocity for Poiseuille flow as \mathbf{u}_{ext} [87]. The nondimensional momentum and charge transport equations become

$$\frac{D^* \mathbf{u}^*}{D^* t^*} = -\nabla^* P^* + \frac{1}{\text{Re}} \nabla^{*2} \mathbf{u}^* - X \rho_c^* \nabla^* \varphi^*, \quad (10)$$

$$\frac{\partial^* \rho_c^*}{\partial^* t^*} + \nabla^* \cdot \left[\left(\frac{|\mathbf{u}_{\text{ext}}|}{u_{\text{drift}}} \mathbf{u}^* - \nabla^* \varphi^* \right) \rho_c^* - \frac{1}{F_e} \nabla^* \rho_c^* \right] = 0, \quad (11)$$

where the Reynolds number is $\text{Re} = \frac{\rho |\mathbf{u}_{\text{ext}}| H}{\mu}$ and $X = \frac{\rho_0 \Delta \varphi_0}{\rho |\mathbf{u}_{\text{ext}}|^2}$ is the ratio of the electrical force to the inertial force [106]. Since Re is essentially the ratio of inertia to viscous forces, and X is the ratio of the electrical force to the inertial force, the product of these (denoted as Y) is the ratio of the electrical force to the viscous force:

$$Y = X \times \text{Re} = \frac{\rho_0 \Delta \varphi_0 H}{\mu |\mathbf{u}_{\text{ext}}|} = \frac{\rho_0 \Delta \varphi_0}{|\tau|}, \quad (12)$$

where τ is the shear stress $\tau = \mu \frac{u_{\text{ext}}}{H}$. In Couette flow τ = constant ($\mathbf{u}_{\text{ext}} = u_{\text{wall}} \mathbf{e}_x$); while in Poiseuille flow, the average value in the channel flow is used hereafter ($\mathbf{u}_{\text{ext}} = u_{\text{center}} \mathbf{e}_x$ and H replaced by half-height $H/2$), where \mathbf{e}_x is a unit vector in the x direction. Detailed interpretation of Y and other NSE terms in the 2D EC cross flow scenario can be found elsewhere [87].

III. SYSTEM LINEARIZATION AND INITIALIZATION

In flow stability problems, the initial linear growth region can be described by the linearized governing equations. The dimensional variables can be written as a summation of the base state (denoted with an overbar) and perturbation (denoted with prime), i.e., $u = \bar{u} + u'$, $P = \bar{P} + P'$, $\varphi = \bar{\varphi} + \varphi'$, and $\rho_c = \bar{\rho}_c + \rho_c'$ [47]. The base-state variables are only functions of z . Substituting these expressions into Eqs. (1)–(4), subtracting the governing equations for the base states, and truncating the second-order perturbation terms yields the linear system:

$$\nabla \cdot \mathbf{u}' = 0, \quad (13)$$

$$\rho \frac{\partial \mathbf{u}'}{\partial t} + (\mathbf{u}' \cdot \nabla) \bar{\mathbf{u}} + (\bar{\mathbf{u}} \cdot \nabla) \mathbf{u}' = -\nabla P' + \mu \nabla^2 \mathbf{u}' - (\rho_c' \nabla \bar{\varphi} + \bar{\rho}_c \nabla \varphi'), \quad (14)$$

$$\frac{\partial \rho_c'}{\partial t} + \nabla \cdot [(\bar{\mathbf{u}} - \nabla \bar{\varphi}) \rho_c' + (\mathbf{u}' - \nabla \varphi') \bar{\rho}_c - D_c \nabla \rho_c'] = 0, \quad (15)$$

$$\nabla^2 \varphi' = -\frac{\rho_c'}{\varepsilon}, \quad (16)$$

which can be written symbolically as

$$\frac{d\boldsymbol{\gamma}}{dt} = \mathbf{L}\boldsymbol{\gamma}, \quad (17)$$

where $\boldsymbol{\gamma}$ is the vector of unknowns, and \mathbf{L} is the linear differential operator.

For periodic boundary conditions in the x and y directions, the normal modes take the form

$$\boldsymbol{\gamma} = W(z) f(x, y) e^{i\omega t}, \quad (18)$$

where $\boldsymbol{\gamma}$ represents any flow variable (\mathbf{u}' , p' , ρ_c' , φ'); ω is the eigenvalue of the spatial-differential matrix \mathbf{L} , and $W(z) f(x, y)$ is the corresponding eigenfunction. The choice of the normal modes depends on the initial perturbation (initial conditions).

To test the accuracy of the numerical approach, a solution to the hydrostatic base state is obtained and compared to the analytical solution for low and high values of C [92,107], as shown in Fig. 1. Without initial perturbation, the system is hydrostatic, and the electrical properties are one-dimensional in the z direction. The boundary conditions are summarized in Table I of the supplementary materials [108].

To obtain various equilibrium solutions, for example, as shown in Fig. 2, different initialization (initial perturbation) schemes are applied to the hydrostatic base state. The initial perturbation used in the simulations has a form similar to the eigenfunction of the normal mode $W(z) f(x, y)$. To satisfy the continuity condition [Eq. (13)], the initial velocity field is described as

$$u_z = W(z) f(x, y), \quad u_x = \frac{1}{a^2} \frac{\partial^2 u_z}{\partial x \partial z}, \quad u_y = \frac{1}{a^2} \frac{\partial^2 u_z}{\partial y \partial z}, \quad (19)$$

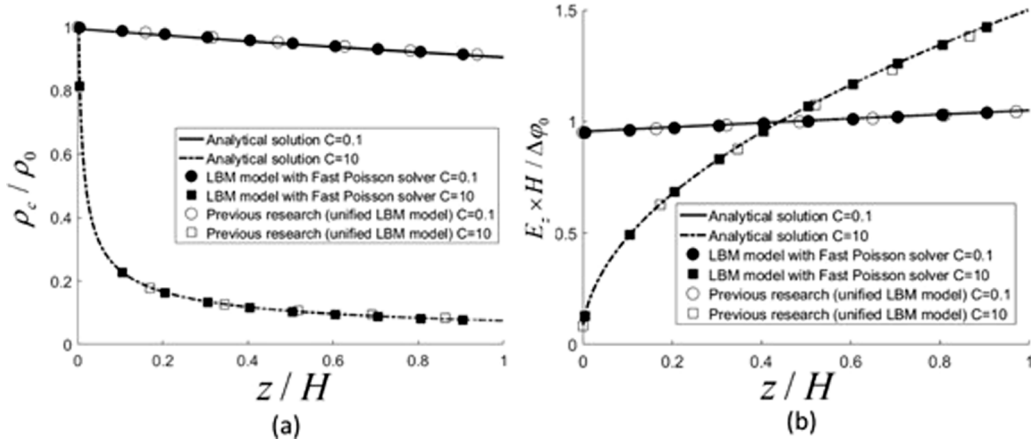


FIG. 1. Hydrostatic solution comparison of the TRT LBM and fast Poisson solver [87,97], unified SRT LBM [52], and the analytical solution [92,107] for $C = 0.1$ and $C = 10$, $Fe = 4000$. (a) Charge density and (b) electric field.

where a depends on the wavelengths in x and y directions and satisfies

$$\left(\frac{\partial^2}{\partial x^2} + \frac{\partial^2}{\partial y^2}\right)f(x, y) = -a^2 f(x, y). \quad (20)$$

The initial perturbation for a rolling pattern (2D) is taken to be

$$u_x = 0, \quad (21)$$

$$u_y = -\frac{dW(z)}{dz} \frac{1}{a^2} \frac{2\pi}{L_y} \sin(2\pi y/L_y), \quad (22)$$

$$u_z = W(z) \cos(2\pi x/L_y), \quad (23)$$

where $W(z)$ is chosen to satisfy the no-slip boundary conditions at the walls, and L_y is the wavelength in the y direction

(spanwise). The initial perturbation for a square pattern (3D) is taken to be

$$u_x = -\frac{dW(z)}{dz} \frac{1}{a^2} \frac{2\pi}{L_x} \sin(2\pi x/L_x), \quad (24)$$

$$u_y = -\frac{dW(z)}{dz} \frac{1}{a^2} \frac{2\pi}{L_y} \sin(2\pi y/L_y), \quad (25)$$

$$u_z = W(z)[\cos(2\pi x/L_x) + \cos(2\pi y/L_y)]. \quad (26)$$

For the square patterns $L_x = L_y$, and from Eq. (20):

$$a = 2\pi/L_y. \quad (27)$$

The initial perturbation for the hexagon pattern (3D) is taken to be

$$u_x = -\frac{dW(z)}{dz} \frac{4\pi}{3\sqrt{3}Lc^2} \sin\left(\frac{2\pi x}{\sqrt{3}L}\right) \cos\left(\frac{2\pi y}{3L}\right), \quad (28)$$

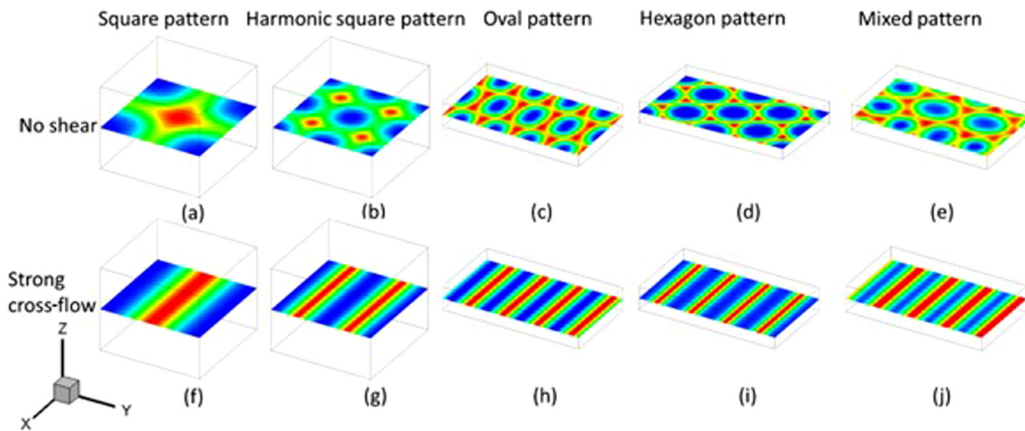


FIG. 2. Contours of u_z at $z = H/2$ for the equilibrium states (a–e) without cross flow, and (f–j) with cross flow sufficient for pattern transition. For different electrical Rayleigh numbers, domain sizes, and initial perturbations (initial conditions), square patterns, oval patterns, hexagon patterns, and mixed patterns are established. Strong cross flow in the x direction is applied to the equilibrium states (a–e), resulting in the 3D transition to 2D streamwise vortices.

$$\begin{aligned}
u_y &= -\frac{dW(z)}{dz} \frac{4\pi}{9Lc^2} \left[\cos\left(\frac{2\pi x}{\sqrt{3}L}\right) + 2\cos\left(\frac{2\pi y}{3L}\right) \right] \\
&\quad \times \sin\left(\frac{2\pi y}{3L}\right), \quad (29) \\
u_z &= \frac{1}{3}W(z) \left[2\cos\left(\frac{2\pi x}{\sqrt{3}L}\right) \cos\left(\frac{2\pi y}{3L}\right) + \cos\left(\frac{4\pi y}{3L}\right) \right], \quad (30)
\end{aligned}$$

where L is the length of the side of the hexagon and the parameter $c = \frac{4\pi}{3L}$ to satisfy Eq. (20).

To satisfy the wall-bounded no-slip boundary condition in the z direction, we use

$$W(z) = [\cos(2\pi z/H) - 1]\varepsilon, \quad (31)$$

where $\varepsilon = 10^{-3}$ is the perturbation magnitude, taken to be the same as in previous 2D analyses [87,97].

IV. DYNAMIC MODE DECOMPOSITION

The DMD analysis is first used to study the linear growth and later to analyze the nonlinear transition region. To study the coherent structures leading to flow instability, we perform DMD on the numerical data for u_z . DMD reconstructs the complex flow system using the linear growth approximation between snapshots of numerical solutions [98]; DMD examines the coherent flow structures and can be used as a tool for flow field predictions and stability analysis. A continuous linear dynamical system [Eq. (17)] can be described by an analogous time-discretized system at intervals Δt :

$$\gamma_{k+1} = \mathbf{A}\gamma_k, \quad (32)$$

where

$$\mathbf{A} = \exp(\Delta t \mathbf{L}), \quad (33)$$

and γ_k is any flow variable (\mathbf{u}' , p' , ρ_c' , φ') at a time step k . The operator \mathbf{L} is a spatial differential matrix of the continuous-time dynamical system, as in Eq. (17). The solution to the discrete-time system can be expressed in terms of eigenvalues λ_j and corresponding eigenvectors ξ_j of the discrete-time mapping matrix \mathbf{A} :

$$\gamma_k = \sum_{j=1}^r \xi_j \lambda_j^k b_j = \boldsymbol{\xi} \mathbf{\Lambda}^k \mathbf{b}, \quad (34)$$

where \mathbf{b} contains the coefficients of the perturbation (initial conditions) γ_1 in the eigenvector basis, such that $\gamma_1 = \boldsymbol{\xi} \mathbf{b}$, r is the rank of the reduced eigenmodes, $\boldsymbol{\xi}$ is the matrix whose columns are the eigenvectors ξ_j , and $\mathbf{\Lambda}^k$ is a diagonal matrix whose entries are the eigenvalues λ_j raised to the power of k .

The results obtained by the DMD algorithm based on the data collected from the numerical simulations can be compared to the values calculated by linear stability analysis in the linear growth region.

With the low-rank approximation of both the eigenvalues and the eigenvectors, the projected future solution can be

constructed:

$$\boldsymbol{\gamma}(t) \approx \sum_{j=1}^r \xi_j \exp(\omega_j t) b_j = \boldsymbol{\xi} \exp(\boldsymbol{\Omega} t) \mathbf{b}, \quad (35)$$

where $\omega_j = \ln(\lambda_j)/\Delta t$ and $\mathbf{b} = \boldsymbol{\xi}^\dagger \boldsymbol{\gamma}_1$, $\boldsymbol{\xi}$ is the matrix whose columns are the DMD eigenvectors ξ_j , superscript \dagger is the Moore-Penrose pseudoinverse, and $\boldsymbol{\Omega}$ is a diagonal matrix whose entries are the eigenvalues ω_j . The details of the implementation of DMD is included in the supplementary materials [108].

V. RESULTS AND DISCUSSION

The TRT LBM approach is used to solve the transport equations for fluid flow and charge density, coupled to a fast Poisson solver for the electric potential [87,97]. The solver is extended to 3D for the differential equations [Eqs. (1)–(4)], the simulations are performed using the initial perturbations (i.e., initial conditions) as per Eqs. (21)–(23) for the rolling pattern, Eqs. (24)–(26) for the square pattern, and Eqs. (28)–(30) for the hexagon pattern and mixed patterns. The equilibrium state was obtained when the flow became steady. The numerical code implementation is in SI units, and the physical constants are determined by the nondimensional parameters. The numerical method is implemented in C++ using CUDA GPU computing. FFT and IFFT operations use the cuFFT library [109–111]. All variables are computed with double precision to reduce truncation errors. The numerical method was shown to be 2nd order accurate in space [97]. Error analysis is provided in supplementary materials [108]. The code can be found at Ref. [112].

A. Electroconvection vortices and transition to rolls:

General patterns

The equilibrium patterns of EC flow fields without cross flow were obtained using the initial perturbations described in Sec. III. The resulting patterns depend on the nondimensional parameter T and the domain size; the latter determines the wavelengths of the vortices. Note that, the rolling, square, and hexagon patterns have been previously observed for the EC system [34,35,70] and the EKI systems [53,91]. Figures 2(a)–2(e) show the equilibrium states of u_z at $z = H/2$. The values $C = 10$, $M = 10$, and $F_e = 3500$ were held constant for each condition. The simulations were carried to $T = 170$ for u_z plotted in Figs. 2(a) and 2(c)–2(e), and to $T = 833$ for u_z in Fig. 2(b). The domain sizes and initial perturbation for the simulations plotted in Figs. 2(a) and 2(b) are the same [Eqs. (24)–(26)], and therefore u_z in Fig. 2(b) is the harmonic of u_z in Fig. 2(a) and develops at a higher value of T . For cases given in Figs. 2(c)–2(e), different domain sizes with a hexagon initial perturbation [Eqs. (28)–(30)] were used. When sufficiently strong Couette-type cross flow in the x direction was applied to the 3D structures, the transition to 2D streamwise rolling patterns occurs for all initial perturbations scenarios [Figs. 2(f)–2(j)].

To study the mechanism for the transition of 3D vortices to streamwise vortices, we consider the simplest scenario, i.e., the case where the equilibrium state is a single period square pattern, see Fig. 2(a). Further generalization of

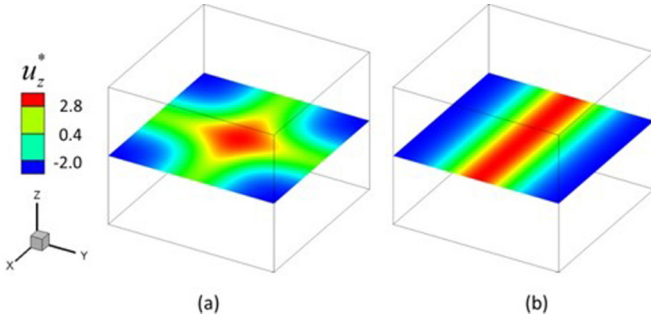


FIG. 3. Contours of u_z^* at $z = H/2$ for initial perturbation of (a) a square pattern and (b) a rolling pattern with $T = 170$, $C = 10$, $M = 10$, and $F_e = 3500$.

transition for other patterns can be a subject of future work. The physical domain used in the simulation is given by $L_x = L_y = 1.22m$ and $H = 1m$; this limits the wave number to $k_x = k_y = 2\pi/L_x \approx 5.15(1/m)$ [34,47]. The electrical Nusselt number, $Ne = I/I_0$, serves as a flow stability criteria, where I is the cathode current for a given solution and I_0 is the cathode current for the base-state solution without EC vortices [34,43]; thus, $Ne > 1$ when EC vortices exist. Note that the use of current as the metric for EC convection has been used in the studies of related overlimiting current in electrokinetic systems [48]. The transition to EC chaotic flow [57] at higher values of the forcing term is not considered in this paper. For the EC problem with the cross flow, the stability largely depends on Y [87]; thus, in this analysis Y is varied, while other nondimensional parameters are held constant at $T = 170$, $C = 10$, $M = 10$, and $F_e = 3500$.

B. Perturbation of the hydrostatic base state with square and rolling patterns

An initial perturbation was applied to the hydrostatic base state after the one-dimensional electrical property profiles were established, as shown in Fig. 1. Figure 3 shows that for $T > T_c$, the 2D perturbation [Eqs. (21)–(23)] leads to the development of a rolling pattern with flow only in the y and z directions, while the 3D square perturbation [Eqs. (24)–(26)]

leads to a square pattern with velocities in all three directions. Figure 4 shows the evolution of the maximum u_z for the first $t^* = 0 \sim 5$ after the perturbation is applied (nondimensional time scale is obtained via normalization by $H^2/(\mu_b \Delta \phi_0)$, as described in Sec. II). Both the rolling pattern and square pattern have the same nondimensional linear growth rate [~ 0.896 as ω in Eq. (18)], which agrees with the previously reported linear stability analysis [47] and the unified SRT LBM numerical model [34] (the case with $T = 170$, $C = 10$, $M = 10$, and $F_e = 4000$ is included in Supplemental Material for validation [108]). After about $t^* = 5$ from the initial perturbation, the growth rate curves for square and rolling vortices patterns diverge. Although the maximum u_z^* is greater for the square pattern, the charge transport (based on $Ne = I/I_0$) for rolling patterns is greater, as shown later in Figs. 17 and 18.

To study the dynamics of the system, DMD is performed based on the numerical data of the square pattern perturbation case from $t^* = 0-2.5$ at intervals of $\Delta t^* = 0.125$. Figure 5 shows the eigenvalues λ of the discrete-time mapping matrix \mathbf{A} as in Eq. (33) and the logarithmic mapping of the eigenvalues ω of the matrix \mathbf{L} as in Eq. (17). The eigenvalues λ are shown in relationship to the unit circle (dashed line); most of the values are inside the circle and therefore represent stable dynamic modes. Three unstable modes (solid dots) with positive growth rates are found. The unstable modes with $\lambda_i = 0$ suggest that these modes do not oscillate.

The three unstable modes with positive growth rates dominate the flow pattern. Figure 6 shows the eigenvectors of these three modes at $t^* = 2.5$, plotted on the plane $z = H/2$. The plots show square patterns with different wavelengths and phase shifts. Although the mode $\omega_r = 0.908$ has a slower growth rate, it contains $>99\%$ of the energy of the perturbation (its initial amplitude of $b = 1.826$ is much greater than that of the others). The overall growth rate (~ 0.896) from Fig. 4 is very close to the growth rate of this dynamic mode shown in Fig. 6(c). The comparison of the dynamic modes Figs. 6(a)–6(c) and simulation solution Fig. 6(d) verifies that the dynamic mode $\omega_r = 0.908$ dominates the flow system. The growth rates of rolling and square patterns are similar to each other, which was also observed in the previous report [34].

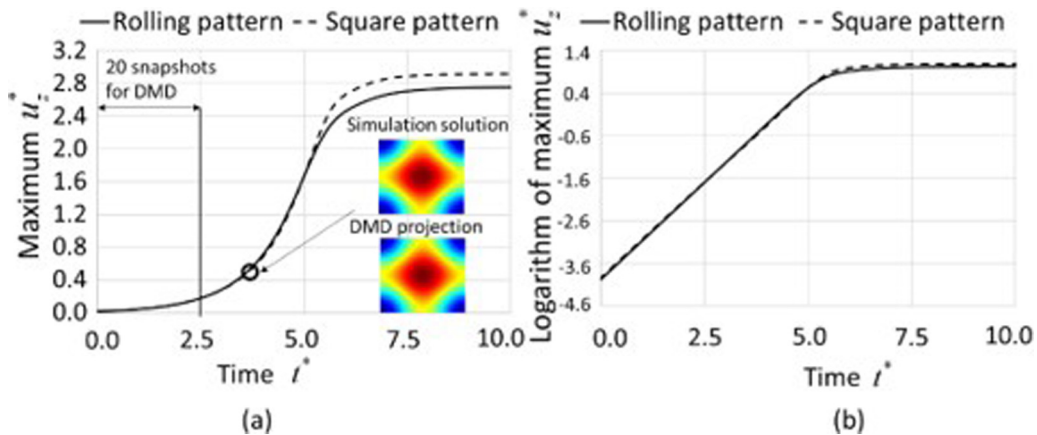


FIG. 4. Time evolution of maximum u_z^* for the rolling pattern and square pattern in (a) a linear scale and (b) a logarithmic scale. Both patterns have similar growth rates (~ 0.896) in the linear growth region ($t^* = 0 \sim 5$). The DMD algorithm-based solutions in the interval $t^* = 0-2.5$ project the state as shown at $t^* = 3.75$ using Eq. (35).

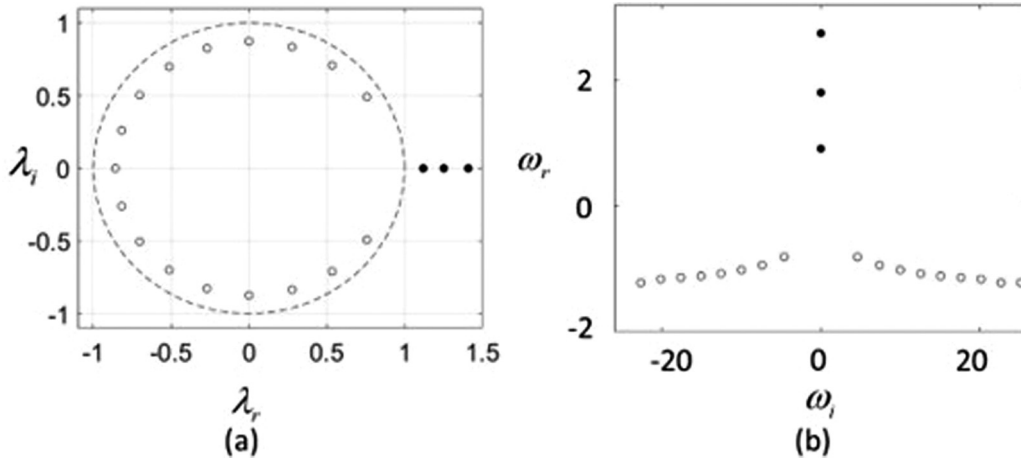


FIG. 5. (a) Eigenvalues of the discrete-time mapping matrix \mathbf{A} and (b) logarithmic mapping of eigenvalues of \mathbf{L} . The eigenvalues outside the unit circle, whose logarithmic value has a real component ω_r greater than 0, represent the unstable dynamic modes. The logarithmic mapping of the eigenvalue \mathbf{L} indicates the growth rate of each dynamic mode.

C. Perturbation of the hydrostatic base state with the inclusion of a cross flow

In the second scenario, we consider the EC problem with an initial perturbation applied to the hydrostatic base state after a cross-flow field in the x direction is developed. Cases for two cross flows are studied. Only the square initial perturbation [Eqs. (24)–(26)] is considered.

Couette flow is obtained by applying the speed u_{wall} to the upper wall while holding the bottom wall fixed. Poiseuille flow driven by a body force representing a pressure drop, F_p , so that the center plane velocity is $u_{\text{center}} = \frac{1}{2\mu} (\frac{H}{2})^2 F_p$. The values of u_{wall} and u_{center} are both nondimensionalized by u_{drift} such that $u_{\text{wall}}^* = u_{\text{wall}}/u_{\text{drift}}$ and $u_{\text{center}}^* = u_{\text{center}}/u_{\text{drift}}$.

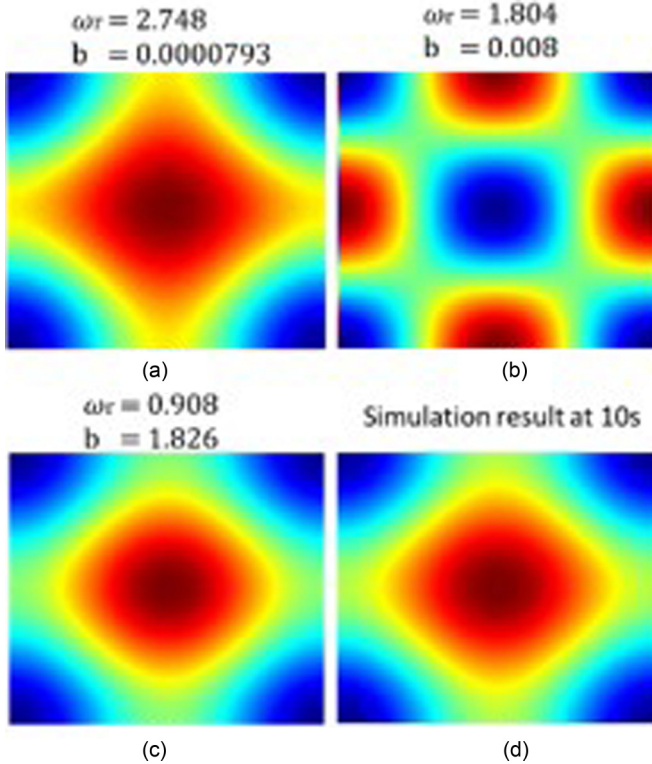


FIG. 6. Unstable dynamic modes visualized by u_z at $z = H/2$. (a–c) Three unstable DMD modes; (c) perturbation has the greatest of projection ($b = 1.826$) on this eigenmode; therefore, it contains most of the energy of the system; (d) the simulated u_z at $z = H/2$. The growth rate of mode (c) $\omega_r = 0.908$ is close to the general growth rate of the entire system (~ 0.896) observed in Fig. 4.

Figure 7 shows the evolution of maximum u_z^* and Ne for both cases. For $t^* < 5$ after the initial perturbation [Eqs. (24)–(26)], the growth is linear, and the growth rate of ~ 0.896 is the same for all solutions. The growth rate is the same with and without cross flow, because the cross flow does not affect the streamwise vortices and, as is shown in Fig. 4, the streamwise vortices grow at the same rate as the 3D square patterns. Previously reported linear stability analysis [85] predicts that the cross flow does not affect the growth rate of longitudinal rolls, but that it decreases the growth rate of traverse rolls. The effect of cross flow on the growth rate of the traverse rolls is also observed from the simulations, as shown in the supplementary material [108]. When the square pattern initial perturbation is applied, both longitudinal and traverse rolls coexist. Since the convolution between these orthogonal rolls decreases the growth rate of each pattern (square and rolling patterns have the same growth rate, as shown in Fig. 4), the weakening effect of the cross flow on the traverse rolls may be compensated by the longitudinal rolls.

At time $t^* \sim 5$, the growth rate curves diverge to reach different equilibrium states for different cross-flow scenarios and perturbation schemes. With weak cross flow ($u_{\text{wall}}^* = 1.6$ for Couette flow, $u_{\text{center}}^* = 1.68$ for Poiseuille flow), the final solutions exhibit oblique 3D vortex structures; both transverse and regular longitudinal rolls coexist. The maximum values of u_z^* for these oblique 3D vortices are greater than for cases with rolling patterns. For strong cross flow ($u_{\text{wall}}^* = 4$ for Couette and $u_{\text{center}}^* = 3.84$ for Poiseuille flow), the systems develop directly into a longitudinal rolling pattern regardless of the initial perturbation; i.e., transverse rolls do not exist even when they are included in the initial perturbation contained

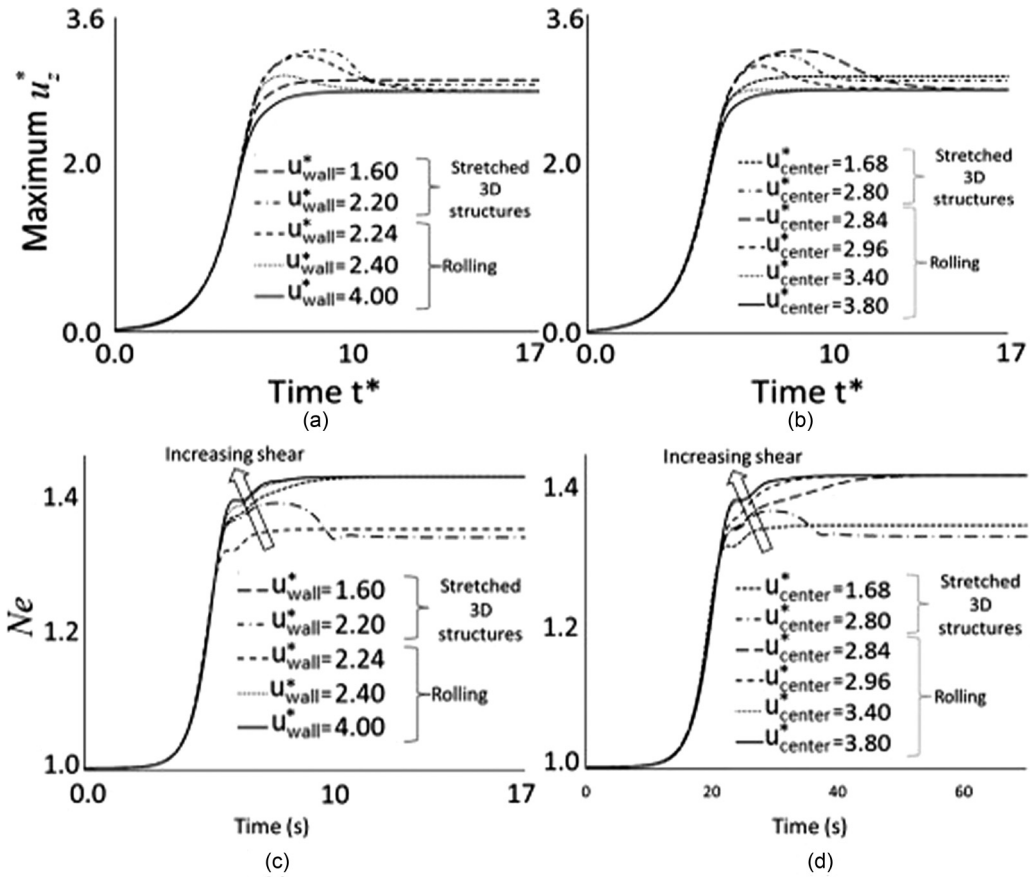


FIG. 7. Time evolution of maximum u_z^* and Ne for (a, c) Couette cross flow and (b, d) Poiseuille cross flow. Maximum u_z^* have similar growth rates (~ 0.896) in the linear growth region ($t^* = 0 \sim 5$). The square pattern initial perturbation scheme [Eqs. (24)–(26)] is used. For strong cross flow, the systems develop into longitudinal rolling patterns. For the weak cross flow, the systems develop into oblique 3D structures with both transverse and longitudinal structures.

in the square pattern. The maximum u_z of the streamwise vortices in the cross-flow case is the same as for the 2D rolling vortices without cross flow, as shown in Fig. 4; in other words, streamwise vortices are superimposed onto the base-state cross-flow solution. For the final steady state (oblique 3D or 2D rolling vortices), the solutions with and without cross flow bifurcate at $u_{wall}^* = 2.2$ for Couette and $u_{center}^* = 2.8$

for Poiseuille flow at about $t^* = 5$. Before reaching an equilibrium state, the cases with the moderate cross flow exhibit an intermediate state where the maximum u_z^* can be greater than the final longitudinal rolling pattern case ($u_z^* = 2.75$) or even the square pattern case with both transverse and longitudinal rolls ($u_z^* = 2.91$). After reaching the peak, in each case u_z^* decreases to an equilibrium solution corresponding to the

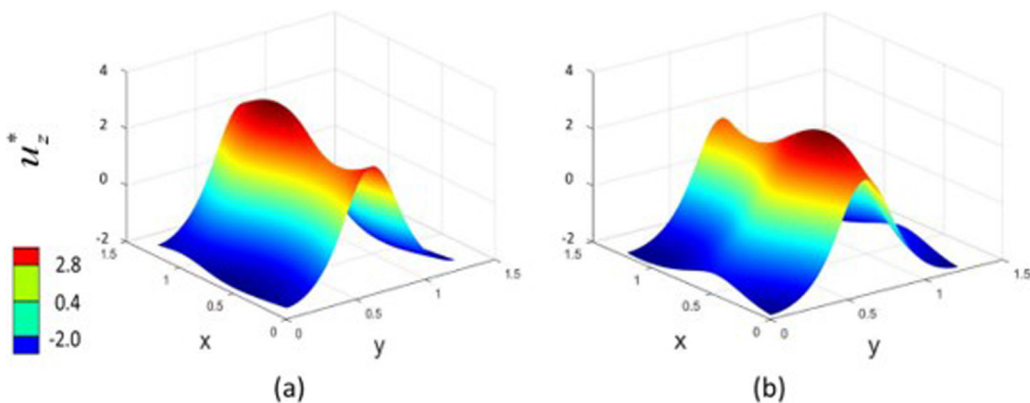


FIG. 8. Contours of u_z^* for $z=H/2$, $t = 7.5$: (a) Couette flow $u_{wall}^* = 2.24$; (b) Poiseuille flow $u_{center}^* = 2.84$. The color map corresponds to the values of u_z , which is also given by the vertical axis.

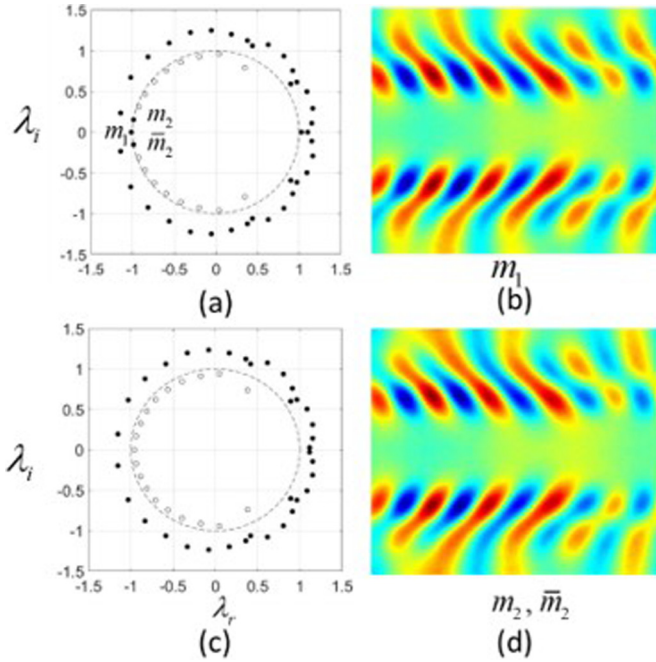


FIG. 9. Eigenvalues λ_i for u_z^* in linear growth region ($t^* = 0-7$) for Couette cross flow [(a) $u_{\text{wall}}^* = 2.20$ and (c) $u_{\text{wall}}^* = 2.24$]. Three additional unstable dynamic modes in $u_{\text{wall}}^* = 2.20$ case change the equilibrium solution from a rolling pattern to oblique 3D structures. The corresponding eigenvectors sliced at $z = H/2$ are shown in (b) mode m_1 and (d) mode m_2 and \bar{m}_2 .

cross-flow strength. For the intermediate cross-flow cases, the systems first develop oblique 3D structures similar to the weak cross-flow cases, and then transition to longitudinal rolling vortices (for Couette flow at $u_{\text{wall}}^* = 2.24$ and 2.40 ; for Poiseuille flow at $u_{\text{center}}^* = 2.84$, 2.96 , and 3.40), as shown in Fig. 8. For strong cross flow (for Couette flow at $u_{\text{wall}}^* = 4$; for Poiseuille flow at $u_{\text{center}}^* = 3.8$) the flows develop directly into longitudinal 2D rolling patterns.

Unlike the evolution of the maximum u_z^* , Ne always increases during the transition from 3D to 2D vortices [Figs. 7(c)–7(d)]. However, when the cross flow is not strong enough to suppress the 3D structures, the steady-state value of Ne for the stronger cross flow can be lower than in the weaker cross flow. In the cross flow with suppressed the transverse structures, the system yields a longitudinal rolling pattern with a constant $Ne = 1.41$, independent of the strength or type of cross flow. As with the u_z analysis, the charge transport by the longitudinal vortices is simply superimposed onto the cross flow regardless of the flow profile.

Figure 8 shows u_z^* at $z = H/2$ and $t^* = 7.5$ for (a) Couette cross flow with $u_{\text{wall}}^* = 2.24$ and (b) Poiseuille cross flow with $u_{\text{center}}^* = 2.84$. At this time, the maximum u_z^* reaches its peak value in the nonlinear growth region. Both plots exhibit a dominating longitudinal rolling pattern aligned with the cross flow in the x direction. The transverse vortex is suppressed due to the interaction of the vortex's x velocity components with the cross flow; these interactions are most profound near the walls where x velocity components of the initial 3D vortices are the greatest. For example, in Couette flow, the clockwise vortex of a vortex pair deforms at some oblique angle as the

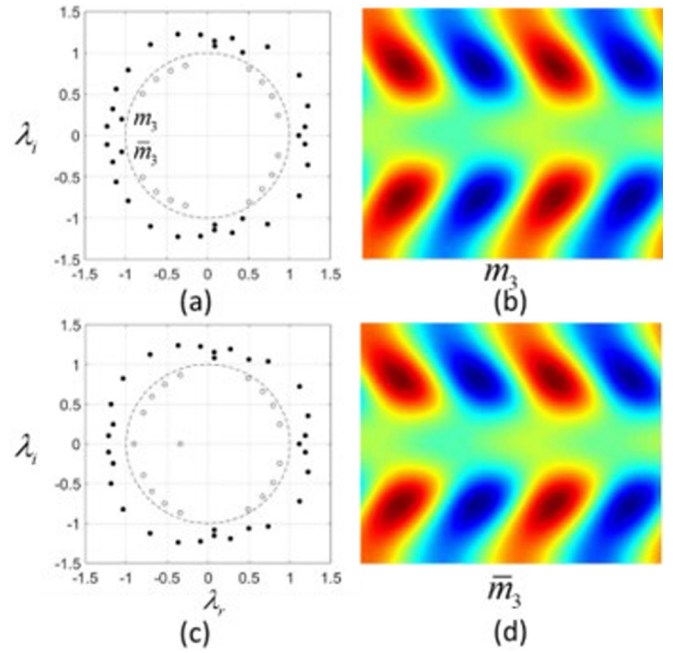


FIG. 10. Eigenvalues λ_i for u_z^* in linear growth region ($t^* = 0-6.25s$) for Poiseuille cross flow [(a) $u_{\text{center}}^* = 2.80$ and (c) $u_{\text{center}}^* = 2.84$]. An additional pair of conjugate unstable dynamic modes in the $u_{\text{center}}^* = 2.80$ case change the equilibrium solution from a rolling pattern to an oblique 3D structure pattern. The corresponding eigenvectors sliced at $z = H/2$ are shown in (b) mode m_3 and (d) mode \bar{m}_3 .

x direction (streamwise) flow accelerates the upper region of the 3D structure and retards the bottom vortex region. This progress is reversed in the case of the counterclockwise rotating vortex of the pair. Eventually, these transverse structures become suppressed, and the systems develop into longitudinal rolling patterns [87]. Since the longitudinal rolling pattern is two dimensional in the y and z directions, it does not interact with the bulk cross flow. For the Poiseuille flow, the mechanism is slightly different; however, the interactions of the vortex structure and the bulk flow exist only in the x direction; thus, y - z structures are not affected by the cross flow; therefore, the streamwise vortices cannot be suppressed by any type of the cross flow.

DMD analysis of the EC vortices in the cross flow was performed using the numerical data of u_z^* in the linear growth region ($t^* = 0-7$ for Couette flow and $t^* = 0-6.25$ for Poiseuille flow) at time intervals of $\Delta t^* = 0.125s$. A greater number of unstable dynamic modes exist in the oblique 3D pattern compared to the rolling pattern. Figure 9 shows the λ for Couette cross flow at (a) $u_{\text{wall}}^* = 2.20$ and (c) $u_{\text{wall}}^* = 2.24$. Similarly, Fig. 10 shows λ for Poiseuille cross flow: (a) $u_{\text{center}}^* = 2.80$ and (c) $u_{\text{center}}^* = 2.84$. As in the u_z^* evolution in hydrostatic base states without cross flow (Figs. 4–6), a perturbation in cross flow arouses several unstable dynamic modes. Most of the dynamic modes are similar in the corresponding flows, resulting in a similar flow field up to the bifurcation point. However, in both cases, the lower velocity flow contains additional unstable modes, i.e., m_1 and the conjugate pair $m_2 - \bar{m}_2$ in Couette cross flow, and mode $m_3 - \bar{m}_3$

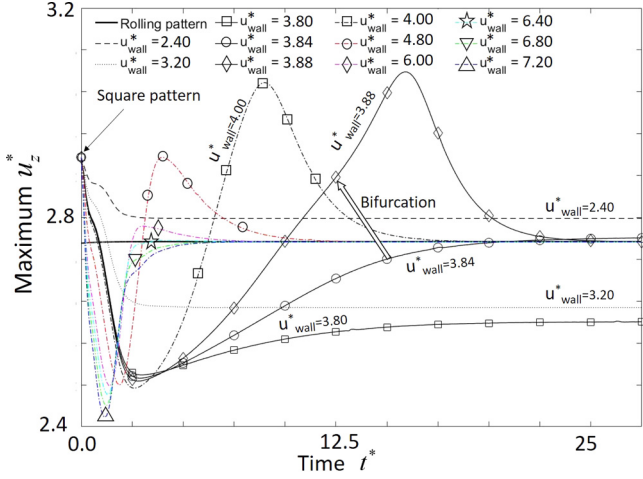


FIG. 11. Time evolution of maximum u_z^* after a finite velocity is applied to the upper wall. For small u_{wall}^* , the maximum u_z^* decreases and reaches a new equilibrium state where oblique 3D structures are observed. For large u_{wall}^* , the maximum u_z^* decreases down to the rolling pattern where longitudinal rolls dominate, after a nonlinear transition. Bifurcation occurs at $u_{wall}^* = 3.88$.

in Poiseuille cross flow. These additional unstable dynamic modes correspond to 3D features changing the stability of the system; they appear in the nonlinear growth region up to the bifurcation point where the curves of weak and strong cross flow start to diverge [see Figs. 7(a) and 7(b)].

D. Pattern transition after the application of cross flow

This section studies the transitions of 3D to 2D patterns by applying the cross flow to already developed square vortex structures, as shown in Fig. 3(a). With weak cross flow, the systems transitions to oblique 3D vortex structures (oblique transverse and regular longitudinal structures coexist). Increasing cross flow yields a longitudinal rolling pattern, i.e., transverse structures are fully suppressed. Figure 11 shows the time evolution of maximum u_z^* in Couette cross flow. For lower cross-flow velocities (e.g., $u_{wall}^* = 2.40$) and, therefore, weak shear stress, the maximum u_z^* decreases to an equilibrium value, which is somewhat greater than that for the rolling pattern flow ($u_{wall}^* = 2.75$). Interestingly, with further increase in u_{wall}^* (e.g., $u_{wall}^* = 3.20$), the equilibrium value of u_z^* may decrease below the value of the rolling pattern. And with even further increasing u_{wall}^* (e.g., $u_{wall}^* = 3.84$), the equilibrium solution develops an oblique 3D structure with maximum u_z that is greater than that of the rolling pattern. However, at $u_{wall}^* = 3.88$, a bifurcation occurs, and the steady-state solution has only 2D streamwise vortices. The transition from 3D to the 2D rolling pattern is marked by a significant increase in u_z^* to a value greater than the original square pattern, before finally decaying to the value of the rolling pattern. This significant increase is a result of kinetic energy transfer from modes with 3D structures to the dominating 2D structures. For larger u_{wall}^* , the peak u_z^* value is reduced, and the time required for pattern transition also decreases. When the applied u_{wall}^* is sufficiently large (e.g., $u_{wall}^* > 6.8$), the maximum value of u_z^* never is above that of the rolling pattern.

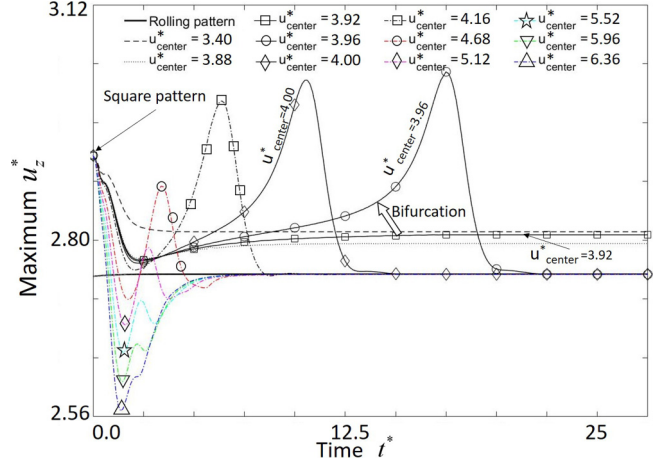


FIG. 12. Time evolution of maximum u_z^* after a uniform body force is applied to the flow field. For small u_{center}^* , the maximum u_z^* decreases and reaches a new equilibrium state where oblique 3D structures are observed. For large u_{center}^* , the maximum u_z^* decreases to the rolling pattern values where longitudinal rolls dominate, after a nonlinear transition. The bifurcation occurs at $u_{center}^* = 3.96$.

Similar behavior is observed for the Poiseuille flow. Figure 12 shows the time evolution of maximum u_z due to an applied uniform body force F_p used to obtain the Poiseuille cross flow. For small u_{center}^* and, therefore, weak applied shear stress (e.g., $u_{center}^* = 3.40$), the maximum u_z^* decays to an equilibrium state with a value greater than that of the rolling pattern (2.75). With increasing F_p (e.g., $u_{center}^* = 3.92$), the

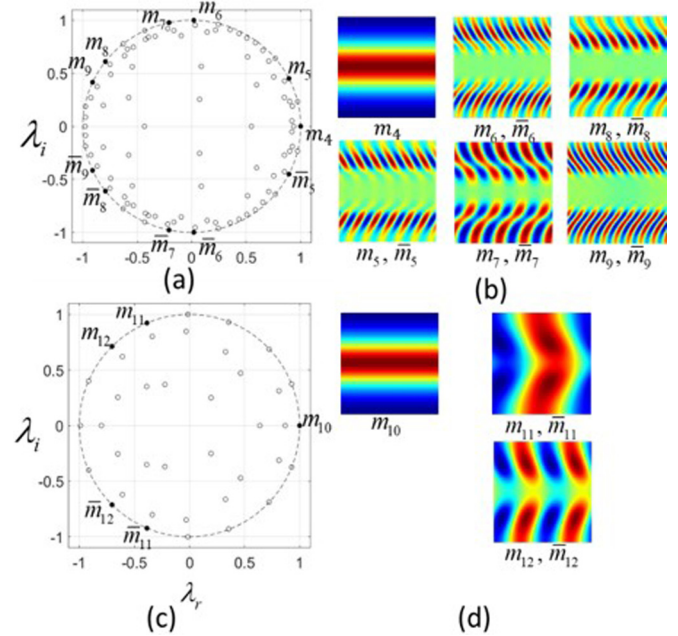


FIG. 13. Eigenvalues λ_i for u_z^* in the transition region for (a) Couette-type cross flow, $u_{wall}^* = 3.84$, and (c) Poiseuille-type cross flow, $u_{center}^* = 3.88$. Unstable dynamic modes change the equilibrium solution from a square pattern to oblique 3D structures. The corresponding eigenvectors sliced at $z = H/2$ are shown in (b), mode $m_4 - \bar{m}_9$, and in (d), mode $m_{10} - \bar{m}_{12}$.

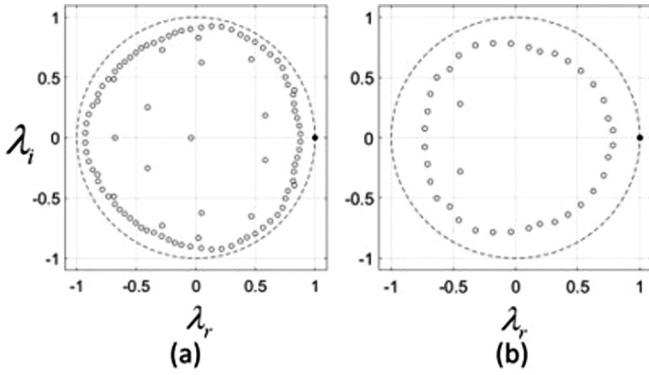


FIG. 14. E eigenvalues λ_i for u_z^* in the transition region for (a) Couette-type cross flow with $u_{\text{wall}}^* = 3.88$, and (c) Poiseuille type cross flow with $u_{\text{center}}^* = 4.16$. The unstable dynamic modes yield the rolling structures.

equilibrium solution develops an oblique 3D structure as the maximum u_z slightly increases after decaying to a minimum value. With u_{center}^* up to 3.92, both oblique transverse and longitudinal structures coexist in the equilibrium solution. However, at $u_{\text{center}}^* = 3.96$, a bifurcation occurs, and the steady-state solution yields 2D streamwise vortices only. The transition from 3D to the 2D rolling pattern is marked by a significant increase in u_z^* to a value greater than the original square pattern before ultimately decaying into the rolling pattern. For large F_p , the peak value of u_z^* is reduced, and the time required for pattern transition also decreases. When

the applied F_p is sufficiently large (e.g., $u_{\text{center}}^* = 5.52$), the maximum value of u_z^* does not exceed the levels above that of the rolling pattern.

To analyze the coherent structures leading to suppression of the instabilities, DMD analysis of the EC in the cross flow was performed using the numerical results in the transition region for $\Delta t^* = 0.25$. Figure 13 shows λ_i for the weak cross flow cases: (a) $u_{\text{wall}}^* = 3.84$ for Couette cross flow, and (c) $u_{\text{center}}^* = 3.88$ for Poiseuille cross flow. The corresponding unstable eigenvectors correspond to the nondecaying coherent flow structures. In addition to the dominant dynamic modes (m_4 and m_{10}) corresponding to the rolling pattern, unstable dynamic modes (m_5-m_9 and $m_{11}-m_{12}$) exist; these are associated with the oblique 3D features. The unstable modes are similar to the ones obtained from the linear growth of perturbation in the cross-flow scenario, see Figs. 9 and 10, which can lead to changes in the stability of the entire system. Figure 14 shows the analysis of the strong cross-flow cases ($u_{\text{wall}}^* = 3.88$ for Couette and $u_{\text{center}}^* = 4.16$ for Poiseuille cross flows). Only a single unstable eigenvalue is observed, which corresponds to rolling pattern eigenvectors m_4 or m_{10} in Fig. 13. The DMD analysis is consistent with the numerical simulation; the EC flow transforms from 3D square to 2D rolling with the strong cross flow. A list of the unstable eigenvalues is included in Table II of the Supplemental Material [108].

Figure 15 shows u_z^* at $z = H/2$ for Couette and Poiseuille cross flow when the maximum value reaches the valley ($t^* = 2.5$, $u_{\text{wall}}^* = 3.88$, and $t^* = 2$, $u_{\text{center}}^* = 4.16$) and peak ($t^* =$

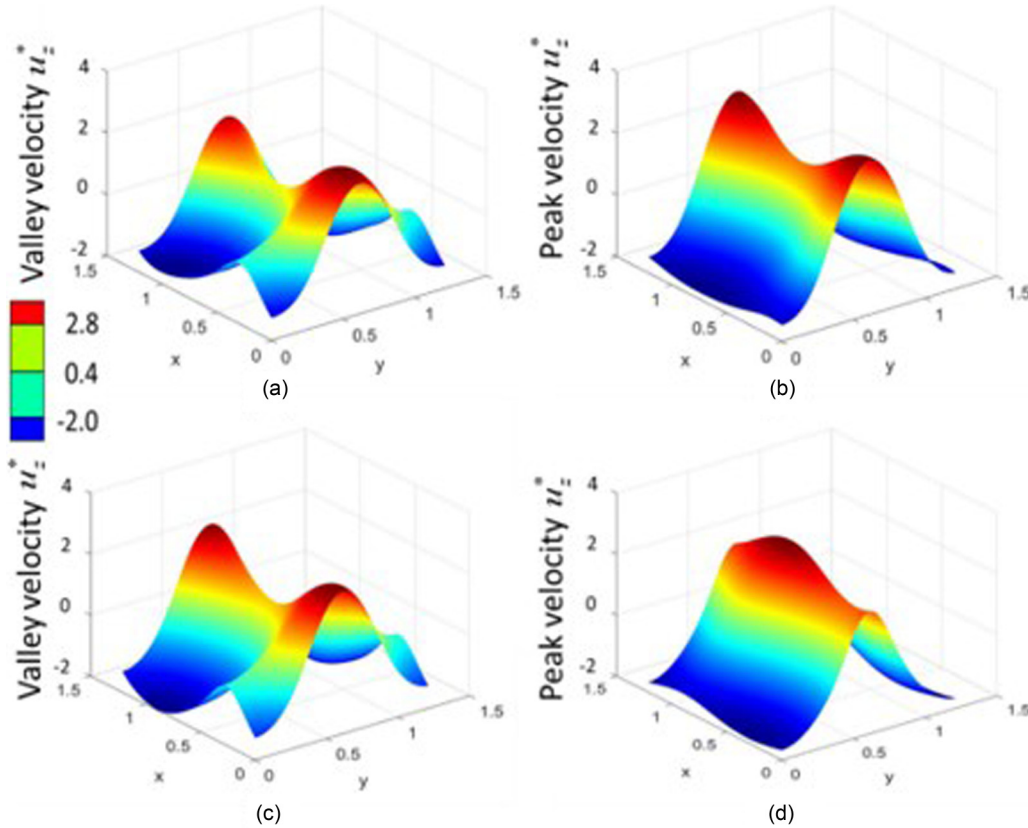


FIG. 15. Contours of valley and peak velocity u_z^* for (a, b) Couette cross flow ($u_{\text{wall}}^* = 3.88$) and (c, d) Poiseuille cross flow ($u_{\text{center}}^* = 4.16$).

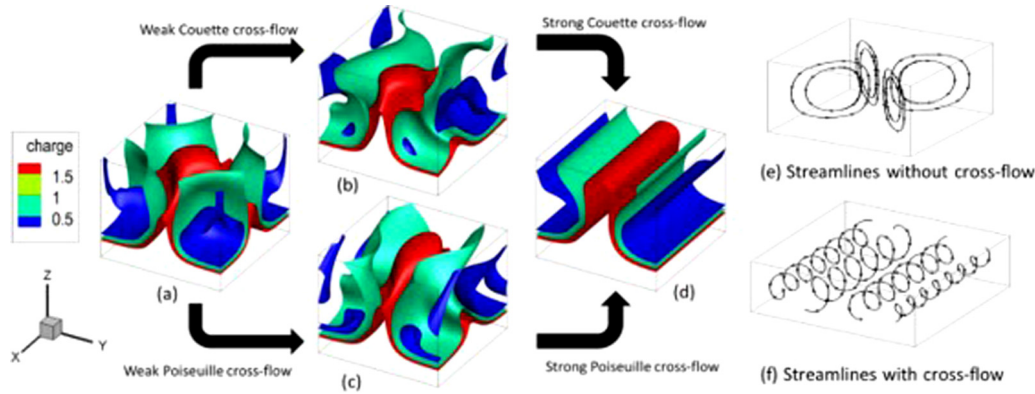


FIG. 16. Isosurfaces of charge density for (a) square pattern without cross flow, (b) $u^*_{wall} = 3.84$, (c) $u^*_{center} = 3.92$, and (d) strong cross flow or rolling pattern. Streamlines (e) without cross flow (circulation streamline) and (f) with strong cross flow (helical streamline). Cross flow is in the x direction.

15.75, $u^*_{wall} = 3.88$ and $t^* = 6.25$, $u^*_{center} = 4.16$), as shown in Figs. 11 and 12. For both types of cross flow, the u^*_z patterns are similar. When the maximum u^*_z is at its valley, oblique 3D structures are more pronounced, while a rolling pattern dominates the flow at the high maximum u^*_z . The transition can be interpreted as energy transfer from one dominant mode to another. Further analysis of the nonlinear transition behavior can be performed by solving for a reduced nonlinear system such as given by the coupled Ginzburg-Landau equations for transverse and longitudinal rolls, similar to the analysis of the effects of cross flow on RBC [74,76,77].

Figure 16 shows the isosurfaces of charge density during the transition from a square to a rolling pattern. Square patterns of charge density are observed at the conditions without cross flow, as shown in Fig. 16(a). When a weak cross flow is applied, the iso-surfaces are obliquely stretched in the x direction, as shown in Figs. 16(b) and 16(c). For strong cross flow, the transverse patterns are suppressed, and only a rolling pattern is observed, see Fig. 16(d). The isosurfaces of charge density are identical for all strong cross-flow cases, and for the rolling pattern perturbation without cross flow. Phenomenologically, the EC system behaves similarly to the RBC system [75]. It is also similar to the 3D EKI in cross flow [91], as the superposition of the motion of the vortices and the major crossflow results in the helical streamline patterns.

Figures 17 and 18 show the dependence of the electrical Nusselt number on the nondimensional parameter Y calculated in the cross-flow direction. Similar to the previous 2D analysis [87], the vortices perpendicular to the cross flow are suppressed. Hysteresis behavior with well-defined bifurcation is observed for both Couette and Poiseuille cross flows. The bifurcation thresholds are $Y_c = 772.73$, $Y_f = 438.14$ for Couette cross flow and $Y_c = 300.75$, $Y_f = 213.90$ for Poiseuille cross flow. At $Ne = 1$ (base state) EC vortices are not present. If $Y > Y_c$, then the square pattern perturbation [Eq. (24)–(26)] results in oblique 3D structures. For $Y < Y_c$, any perturbation results in streamwise rolling vortices as the equilibrium solution. Oblique 3D flow features develop when shear stress is applied to the square pattern. As Y is reduced (shear stress increased), the oblique features persist until $Y = Y_f$. Additional reduction in Y suppresses the features in the transverse direction; only the longitudinal structures are possible. The Ne value is lower in 3D EC vortices; the oblique 3D structures result in decreasing Ne . When Y is close to Y_f , Ne slightly increases before transitioning to the rolling pattern value. This increase of Ne agrees with trends in maximum u_z , as shown in Figs. 11 and 12. The inserts in Figs. 17 and 18 show u_z contour plots at $z = H/2$; the u_z profiles are oblique in the cross-flow direction for both Couette and Poiseuille

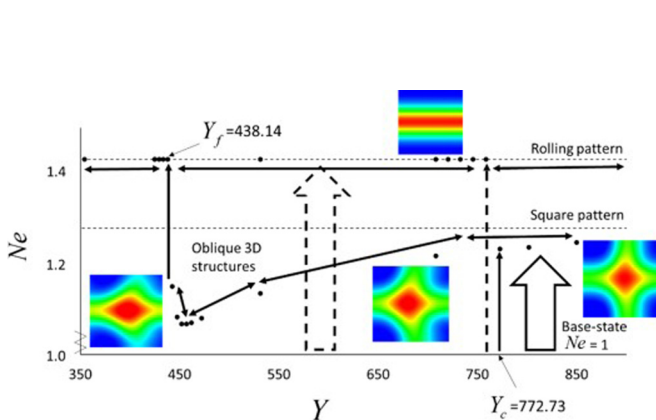


FIG. 17. Hysteresis loop of Ne vs. Y for Couette cross flow. The bifurcation thresholds are $Y_c = 772.73$, $Y_f = 438.14$.

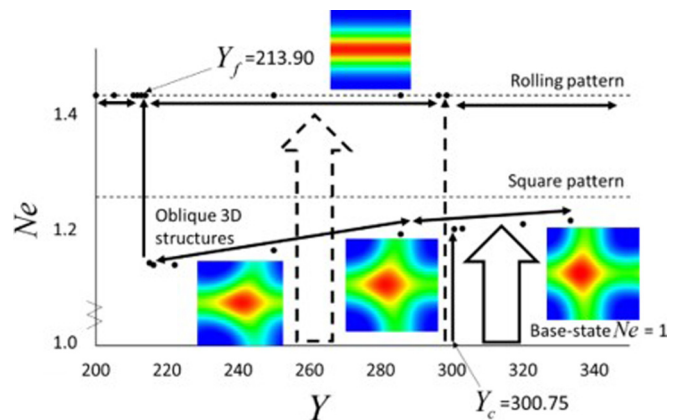


FIG. 18. Hysteresis loop of Ne vs. Y for Poiseuille-type cross flow. The bifurcation thresholds are $Y_c = 300.75$, $Y_f = 213.90$.

cross flows. The hysteresis loop can be closed by introducing a y -directional cross flow to suppress the rolling pattern vortices [87].

VI. SUMMARY AND CONCLUSIONS

To summarize, the results presented in this work consider the 3D interaction between cross flow and electroconvective transport induced by unipolar charge injection. The increased stability by shear observed in this 3D numerical study is consistent with the previous 2D experimental observations [40,68,69] and 2D numerical results [86]. The DMD analysis sheds insight into the interaction of cross flow with the 3D structures and can be compared to the 2D vorticity analysis from previous work [87]. The applied shear organizes the flow into 2D rolls parallel to the mean flow and enhances the convection marked by an increase in Ne , similar to heat convection problem with moderate Rayleigh number [113]. The presented methodologies (3D TRT LBM model, the DMD analysis, and dimensional analysis) can be extended to other convective systems such as RBC, magnetoconvection, and electrokinetic systems

The interactions between the cross flow and electroconvective vortices lead to suppression and disappearance of structures perpendicular to the bulk flow. The numerical modeling of EHD-EC uses a second-order TRT-LBM scheme to solve the flow and charge transport equations coupled to a Fast Poisson Solver for the electrical potential. Shear from Couette and Poiseuille cross flow first stretches the EC cells at oblique angles due to the interaction between the vortices and the bulk flow. The transition to 2D streamwise vortices occurs after a sufficiently high cross-flow velocity is reached. The transition from 3D to 2D equilibrium states is observed independent of the initial perturbation schemes and the domain configurations

considered in this work, i.e., square perturbations and its harmonic, oval, hexagonal, and mixed perturbations. Two transitional scenarios are studied, (i) the cross flow is applied before and (ii) after the EC vortices are established. If the cross flow is applied before the perturbation leading to the formation of EC vortices, then bifurcation occurs at $u^*_{\max} = 2.20$ for Couette flow and $u^*_{\text{center}} = 2.80$ for Poiseuille flow. If the cross flow is applied after the EC vortices are established, then the convective cells are more stable; the bifurcation occurs at $u^*_{\max} = 3.88$ for Couette flow and $u^*_{\text{center}} = 3.96$ for Poiseuille flow.

DMD analysis of the linear growth and the nonlinear transition regions provides insight into the development of the coherent flow structures, predicting the linear behavior, and identifying bifurcation thresholds. The dynamic modes obtained from the linear growth region agree with the global growth rates obtained from the evolution of u^*_z . To parameterize the transition, the nondimensional analysis of the governing equations uses a parameter Y in the momentum equation. Similar to the 2D cases [87], hysteresis in the 3D cases is observed. The bifurcation thresholds are $Y_c = 772.73$, $Y_f = 438.14$ for Couette flow and $Y_c = 300.75$, $Y_f = 213.90$ for Poiseuille flow.

ACKNOWLEDGMENTS

This research was supported by the DHS Science and UK Home Office, Grant No. HSHQDC-15-531 C-B0033; by the National Institutes of Health, Grants No. NIBIB U01 EB021923 and No. NIBIB R42ES026532 subcontract to U.W. This work was facilitated through the use of advanced computational, storage, and networking infrastructure provided by the Hyak supercomputer system at the University of Washington.

-
- [1] S. Chandrasekhar, *Hydrodynamic and Hydromagnetic Stability* (Courier Corporation, North Chelmsford, MA, 2013).
 - [2] P. G. Drazin and W. H. Reid, *Hydrodynamic Stability* (Cambridge University Press, Cambridge, 2004).
 - [3] E. L. Koschmieder, *Bénard Cells and Taylor Vortices* (Cambridge University Press, North Chelmsford, 1993).
 - [4] P. Bergé and M. Dubois, Rayleigh-bénard convection, *Contemp. Phys.* **25**, 535 (1984).
 - [5] M. Krishnan, V. M. Ugaz, and M. A. Burns, PCR in a Rayleigh-Benard convection cell, *Science* **298**, 793 (2002).
 - [6] A. V. Getling, *Rayleigh-Bénard Convection: Structures and Dynamics* (World Scientific, Singapore, 1998), Vol. 11.
 - [7] K. Luo, T.-F. Li, J. Wu, H.-L. Yi, and H.-P. Tan, Mesoscopic simulation of electrohydrodynamic effects on laminar natural convection of a dielectric liquid in a cubic cavity, *Phys. Fluids* **30**, 103601 (2018).
 - [8] C. Marangoni, *Sull'espansione delle gocce d'un liquido galleggianti sulla superficie di altro liquido* (1865).
 - [9] J. W. Gibbs, On the equilibrium of heterogeneous substances (1879).
 - [10] M. G. Velarde and R. K. Zeytounian, *Interfacial Phenomena and the Marangoni Effect* (Springer, Berlin, 2002).
 - [11] H. Hu and R. G. Larson, Marangoni effect reverses coffee-ring depositions, *J. Phys. Chem. B* **110**, 7090 (2006).
 - [12] F. Girard, M. Antoni, and K. Sefiane, On the effect of Marangoni flow on evaporation rates of heated water drops, *Langmuir* **24**, 9207 (2008).
 - [13] J. Borrero, S. Jafarzadeh, M. Schüssler, and S. Solanki, Solar magnetoconvection and small-scale dynamo, *Space Sci. Rev.* **210**, 275 (2017).
 - [14] J.-F. Cossette, P. Charbonneau, P. K. Smolarkiewicz, and M. P. Rast, Magnetically modulated heat transport in a global simulation of solar magneto-convection, *Astrophys. J.* **841**, 65 (2017).
 - [15] A. Y. Gelfgat and O. Zikanov, Computational modeling of magnetoconvection: Effects of discretization method, grid refinement and grid stretching, *Comput. Fluids* **175**, 66 (2018).
 - [16] E. Khomenko, N. Vitas, M. Collados, and A. de Vicente, Three-dimensional simulations of solar magneto-convection including effects of partial ionization, *Astron. Astrophys.* **618**, A87 (2018).
 - [17] M. S. Alam, M. S. H. Mollah, M. A. Alim, and M. N. Uddin, Effect of Hartmann number on magneto-convection in a lid driven square cavity with wavy side wall, in *AIP Conference Proceedings* (AIP Publishing, Melville, NY, 2018), p. 050013.
 - [18] J. Zhang and M. Zhang, On the infinite Prandtl number limit in two-dimensional magneto-convection, *Nonlin. Anal. Real World Appl.* **46**, 313 (2019).

- [19] N. Riley, Magnetohydrodynamic free convection, *J. Fluid Mech.* **18**, 577 (1964).
- [20] K. Pradhan and A. Guha, CFD solutions for magnetohydrodynamic natural convection over horizontal and vertical surfaces, *J. Mol. Liq.* **236**, 465 (2017).
- [21] B. Shankar and I. Shivakumara, Magnetohydrodynamic stability of pressure-driven flow in an anisotropic porous channel: Accurate solution, *Appl. Math. Comput.* **321**, 752 (2018).
- [22] W. Kuang and J. Bloxham, Numerical modeling of magnetohydrodynamic convection in a rapidly rotating spherical shell: weak and strong field dynamo action, *J. Comput. Phys.* **153**, 51 (1999).
- [23] S. Mahmud and R. A. Fraser, Magnetohydrodynamic free convection and entropy generation in a square porous cavity, *Int. J. Heat Mass Transfer* **47**, 3245 (2004).
- [24] M. Sheikholeslami and D. D. Ganji, Ferrohydrodynamic and magnetohydrodynamic effects on ferrofluid flow and convective heat transfer, *Energy* **75**, 400 (2014).
- [25] M. Waqas, M. Farooq, M. I. Khan, A. Alsaedi, T. Hayat, and T. Yasmeen, Magnetohydrodynamic (MHD) mixed convection flow of micropolar liquid due to nonlinear stretched sheet with convective condition, *Int. J. Heat Mass Transfer* **102**, 766 (2016).
- [26] M. Sheikholeslami and S. Shehzad, Magnetohydrodynamic nanofluid convection in a porous enclosure considering heat flux boundary condition, *Int. J. Heat Mass Transfer* **106**, 1261 (2017).
- [27] B. Zaltzman and I. Rubinstein, Electro-osmotic slip and electroconvective instability, *J. Fluid Mech.* **579**, 173 (2007).
- [28] C. Druzgalski, M. Andersen, and A. Mani, Direct numerical simulation of electroconvective instability and hydrodynamic chaos near an ion-selective surface, *Phys. Fluids* **25**, 110804 (2013).
- [29] E. Karatay, C. L. Druzgalski, and A. Mani, Simulation of chaotic electrokinetic transport: Performance of commercial software versus custom-built direct numerical simulation codes, *J. Colloid Interface Sci.* **446**, 67 (2015).
- [30] C. Druzgalski and A. Mani, Statistical analysis of electroconvection near an ion-selective membrane in the highly chaotic regime, *Phys. Rev. Fluids* **1**, 073601 (2016).
- [31] V. S. Pham, Z. Li, K. M. Lim, J. K. White, and J. Han, Direct numerical simulation of electroconvective instability and hysteretic current-voltage response of a permselective membrane, *Phys. Rev. E* **86**, 046310 (2012).
- [32] M. Dennin, G. Ahlers, and D. S. Cannell, Chaotic Localized States near the Onset of Electroconvection, *Phys. Rev. Lett.* **77**, 2475 (1996).
- [33] M. Dennin, G. Ahlers, and D. S. Cannell, Spatiotemporal chaos in electroconvection, *Science* **272**, 388 (1996).
- [34] K. Luo, J. Wu, H.-L. Yi, and H.-P. Tan, Three-dimensional finite amplitude electroconvection in dielectric liquids, *Phys. Fluids* **30**, 023602 (2018).
- [35] K. Luo, J. Wu, H.-L. Yi, L.-H. Liu, and H.-P. Tan, Hexagonal convection patterns and their evolutionary scenarios in electroconvection induced by a strong unipolar injection, *Phys. Rev. Fluids* **3**, 053702 (2018).
- [36] G. I. Taylor, Studies in electrohydrodynamics. I. The circulation produced in a drop by an electric field, Proceedings of the Royal Society of London. Series A. Mathematical and Physical Sciences **291**, 159 (1966).
- [37] D. C. Jolly and J. R. Melcher, Electroconvective instability in a fluid layer, *Proc. R. Soc. London, Ser. A* **314**, 269 (1970).
- [38] B. Malraison and P. Atten, Chaotic Behavior of Instability Due to Unipolar Ion Injection in a Dielectric Liquid, *Phys. Rev. Lett.* **49**, 723 (1982).
- [39] A. Castellanos and P. Atten, Numerical modeling of finite amplitude convection of liquids subjected to unipolar injection, *IEEE Trans. Ind. Appl.* **IA-23**, 825 (1987).
- [40] Z. A. Daya, V. B. Deyirmenjian, and S. W. Morris, Bifurcations in annular electroconvection with an imposed shear, *Phys. Rev. E* **64**, 036212 (2001).
- [41] P. Tsai, Z. A. Daya, and S. W. Morris, Aspect-Ratio Dependence of Charge Transport in Turbulent Electroconvection, *Phys. Rev. Lett.* **92**, 084503 (2004).
- [42] P. Tsai, Z. A. Daya, and S. W. Morris, Charge transport scaling in turbulent electroconvection, *Phys. Rev. E* **72**, 046311 (2005).
- [43] P. Traoré and A. Pérez, Two-dimensional numerical analysis of electroconvection in a dielectric liquid subjected to strong unipolar injection, *Phys. Fluids* **24**, 037102 (2012).
- [44] P. Traoré and J. Wu, On the limitation of imposed velocity field strategy for Coulomb-driven electroconvection flow simulations, *J. Fluid Mech.* **727**, R3 (2013).
- [45] J. Wu, P. Traoré, P. A. Vázquez, and A. T. Pérez, Onset of convection in a finite two-dimensional container due to unipolar injection of ions, *Phys. Rev. E* **88**, 053018 (2013).
- [46] A. Pérez, P. Vázquez, J. Wu, and P. Traoré, Electrohydrodynamic linear stability analysis of dielectric liquids subjected to unipolar injection in a rectangular enclosure with rigid sidewalls, *J. Fluid Mech.* **758**, 586 (2014).
- [47] M. Zhang, F. Martinelli, J. Wu, P. J. Schmid, and M. Quadrio, Modal and non-modal stability analysis of electrohydrodynamic flow with and without cross-flow, *J. Fluid Mech.* **770**, 319 (2015).
- [48] P. Traore, J. Wu, C. Louste, P. A. Vazquez, and A. T. Perez, Numerical study of a plane poiseuille channel flow of a dielectric liquid subjected to unipolar injection, *IEEE Trans. Dielectr. Electr. Insul.* **22**, 2779 (2015).
- [49] J. Wu, A. T. Perez, P. Traore, and P. A. Vazquez, Complex flow patterns at the onset of annular electroconvection in a dielectric liquid subjected to an arbitrary unipolar injection, *IEEE Trans. Dielectr. Electr. Insul.* **22**, 2637 (2015).
- [50] J. Wu, P. Traoré, A. T. Pérez, and P. A. Vázquez, On two-dimensional finite amplitude electro-convection in a dielectric liquid induced by a strong unipolar injection, *J. Electrostat.* **74**, 85 (2015).
- [51] M. Zhang, Weakly nonlinear stability analysis of subcritical electrohydrodynamic flow subject to strong unipolar injection, *J. Fluid Mech.* **792**, 328 (2016).
- [52] K. Luo, J. Wu, H.-L. Yi, and H.-P. Tan, Lattice Boltzmann model for Coulomb-driven flows in dielectric liquids, *Phys. Rev. E* **93**, 023309 (2016).
- [53] I. Rubinstein and B. Zaltzman, Electro-osmotically induced convection at a permselective membrane, *Phys. Rev. E* **62**, 2238 (2000).
- [54] I. Rubinstein and B. Zaltzman, Electro-osmotic slip of the second kind and instability in concentration polarization at

- electrodialysis membranes, *Math. Models Methods Appl. Sci.* **11**, 263 (2001).
- [55] S. M. Rubinstein, G. Manukyan, A. Staicu, I. Rubinstein, B. Zaltzman, R. G. Lammertink, F. Mugele, and M. Wessling, Direct Observation of a Nonequilibrium Electro-Osmotic Instability, *Phys. Rev. Lett.* **101**, 236101 (2008).
- [56] R. Kwak, V. S. Pham, K. M. Lim, and J. Han, Shear Flow of an Electrically Charged Fluid by Ion Concentration Polarization: Scaling Laws for Electroconvective Vortices, *Phys. Rev. Lett.* **110**, 114501 (2013).
- [57] S. M. Davidson, M. B. Andersen, and A. Mani, Chaotic Induced-Charge Electro-Osmosis, *Phys. Rev. Lett.* **112**, 128302 (2014).
- [58] I. Rubinstein and B. Zaltzman, Convective diffusive mixing in concentration polarization: From Taylor dispersion to surface convection, *J. Fluid Mech.* **728**, 239 (2013).
- [59] I. Rubinstein and B. Zaltzman, Equilibrium Electroconvective Instability, *Phys. Rev. Lett.* **114**, 114502 (2015).
- [60] N. Felici, Phénomènes hydro et aérodynamiques dans la conduction des diélectriques fluides, *Rev. Gén. Electr.* **78**, 717 (1969).
- [61] N. Felici and J. Lacroix, Electroconvection in insulating liquids with special reference to uni- and bi-polar injection: a review of the research work at the CNRS Laboratory for Electrostatics, Grenoble 1969–1976, *J. Electrostat.* **5**, 135 (1978).
- [62] J. Schneider and P. Watson, Electrohydrodynamic stability of space-charge-limited currents in dielectric liquids. I. Theoretical study, *Phys. Fluids* **13**, 1948 (1970).
- [63] P. Watson, J. Schneider, and H. Till, Electrohydrodynamic stability of space-charge-limited currents in dielectric liquids. II. Experimental study, *Phys. Fluids* **13**, 1955 (1970).
- [64] P. Atten and R. Moreau, Stabilité électrohydrodynamique des liquides isolants soumis à une injection unipolaire, *J. Mécanique* **11**, 471 (1972).
- [65] J. Lacroix, P. Atten, and E. Hopfinger, Electro-convection in a dielectric liquid layer subjected to unipolar injection, *J. Fluid Mech.* **69**, 539 (1975).
- [66] P. Atten and J. Lacroix, Non-linear hydrodynamic stability of liquids subjected to unipolar injection, *Journal de Mécanique* **18**, 469 (1979).
- [67] P. Atten, Rôle de la diffusion dans le problème de la stabilité hydrodynamique d'un liquide diélectrique soumis à une injection unipolaire forte, *CR Acad. Sci. Paris* **283**, 29 (1976).
- [68] Z. A. Daya, V. Deyirmenjian, S. W. Morris, and J. R. De Bruyn, Annular Electroconvection with Shear, *Phys. Rev. Lett.* **80**, 964 (1998).
- [69] Z. A. Daya, V. Deyirmenjian, and S. W. Morris, Electrically driven convection in a thin annular film undergoing circular Couette flow, *Phys. Fluids* **11**, 3613 (1999).
- [70] T. John, J. Heuer, and R. Stannarius, Influence of excitation wave forms and frequencies on the fundamental time symmetry of the system dynamics, studied in nematic electroconvection, *Phys. Rev. E* **71**, 056307 (2005).
- [71] Á. Buka, N. Éber, W. Pesch, and L. Kramer, Isotropic and anisotropic electroconvection, *Phys. Rep.* **448**, 115 (2007).
- [72] J.-H. Huh, Traveling waves and worms in ac-driven electroconvection under external multiplicative noise, *Phys. Rev. E* **95**, 042704 (2017).
- [73] J.-H. Huh, Electroconvection in one-dimensional liquid crystal cells, *Phys. Rev. E* **97**, 042707 (2018).
- [74] H. Müller, M. Lücke, and M. Kamps, Convective patterns in horizontal flow, *Europhys. Lett.* **10**, 451 (1989).
- [75] A. Mohamad and R. Viskanta, Laminar flow and heat transfer in Rayleigh–Bénard convection with shear, *Phys. Fluids A* **4**, 2131 (1992).
- [76] H. Müller, M. Lücke, and M. Kamps, Transversal convection patterns in horizontal shear flow, *Phys. Rev. A* **45**, 3714 (1992).
- [77] H. Müller, M. Tveitereid, and S. Trainoff, Rayleigh–Bénard problem with imposed weak through-flow: Two coupled Ginzburg–Landau equations, *Phys. Rev. E* **48**, 263 (1993).
- [78] M. Tveitereid and H. W. Müller, Pattern selection at the onset of Rayleigh–Bénard convection in a horizontal shear flow, *Phys. Rev. E* **50**, 1219 (1994).
- [79] X. Nicolas, A. Mojtabi, and J. K. Platten, Two-dimensional numerical analysis of the Poiseuille–Bénard flow in a rectangular channel heated from below, *Phys. Fluids* **9**, 337 (1997).
- [80] P. Carriere and P. A. Monkewitz, Convective versus absolute instability in mixed Rayleigh–Bénard–Poiseuille convection, *J. Fluid Mech.* **384**, 243 (1999).
- [81] Y. Kato and K. Fujimura, Prediction of pattern selection due to an interaction between longitudinal rolls and transverse modes in a flow through a rectangular channel heated from below, *Phys. Rev. E* **62**, 601 (2000).
- [82] H. Zhang, X. Huang, H. Li, and L. Chua, Flow patterns and heat transfer enhancement in low-Reynolds–Rayleigh-number channel flow, *Appl. Therm. Eng.* **22**, 1277 (2002).
- [83] R. Kwak, V. S. Pham, and J. Han, Sheltering the perturbed vortical layer of electroconvection under shear flow, *J. Fluid Mech.* **813**, 799 (2017).
- [84] P. Magnico, Electro-Kinetic Instability in a Laminar Boundary Layer Next to an Ion Exchange Membrane, *Int. J. Mol. Sci.* **20**, 2393 (2019).
- [85] F. Li, B.-F. Wang, Z.-H. Wan, J. Wu, and M. Zhang, Absolute and convective instabilities in electrohydrodynamic flow subjected to a Poiseuille flow: A linear analysis, *J. Fluid Mech.* **862**, 816 (2019).
- [86] P. Traoré, J. Wu, C. Louste, F. D. Olivencia, P. A. Vázquez, and A. T. Pérez, Numerical investigation of electroconvection induced by strong unipolar injection between two rotating coaxial cylinders, *J. Electrostat.* **94**, 60 (2018).
- [87] Y. Guan and I. Novosselov, Numerical analysis of electroconvection in cross-flow with unipolar charge injection, *Phys. Rev. Fluids* **4**, 103701 (2019).
- [88] P. Taylor, Analytical methods in planetary boundary-layer modelling, *Bound. Layer Meteorol.* **8**, 125 (1975).
- [89] D. Etling and R. Brown, Roll vortices in the planetary boundary layer: A review, *Bound. Layer Meteorol.* **65**, 215 (1993).
- [90] H. Kuo, Perturbations of plane Couette flow in stratified fluid and origin of cloud streets, *Phys. Fluids* **6**, 195 (1963).
- [91] S. V. Pham, H. Kwon, B. Kim, J. K. White, G. Lim, and J. Han, Helical vortex formation in three-dimensional electrochemical systems with ion-selective membranes, *Phys. Rev. E* **93**, 033114 (2016).
- [92] R. Chicón, A. Castellanos, and E. Martín, Numerical modelling of Coulomb-driven convection in insulating liquids, *J. Fluid Mech.* **344**, 43 (1997).
- [93] P. Vazquez, G. Georghiou, and A. Castellanos, Characterization of injection instabilities in electrohydrodynamics by numerical modelling: Comparison of particle in cell and flux

- corrected transport methods for electroconvection between two plates, *J. Phys. D Appl. Phys.* **39**, 2754 (2006).
- [94] J. Wu and P. Traoré, A finite-volume method for electrothermoconvective phenomena in a plane layer of dielectric liquid, *Numer. Heat Transfer, Part A* **68**, 471 (2015).
- [95] K. Adamiak and P. Atten, Simulation of corona discharge in point–plane configuration, *J. Electrostat.* **61**, 85 (2004).
- [96] K. Luo, A. T. Pérez, J. Wu, H.-L. Yi, and H.-P. Tan, Efficient lattice Boltzmann method for electrohydrodynamic solid-liquid phase change, *Phys. Rev. E* **100**, 013306 (2019).
- [97] Y. Guan and I. Novosselov, Two relaxation time lattice Boltzmann method coupled to fast fourier transform Poisson solver: Application to electroconvective flow, *J. Comput. Phys.* **397**, 108830 (2019).
- [98] J. N. Kutz, S. L. Brunton, B. W. Brunton, and J. L. Proctor, *Dynamic Mode Decomposition: Data-driven Modeling of Complex Systems* (SIAM, Philadelphia, PA, 2016), Vol. 149.
- [99] P. J. Schmid, Dynamic mode decomposition of numerical and experimental data, *J. Fluid Mech.* **656**, 5 (2010).
- [100] P. J. Schmid, L. Li, M. P. Juniper, and O. Pust, Applications of the dynamic mode decomposition, *Theor. Comput. Fluid Dyn.* **25**, 249 (2011).
- [101] P. J. Schmid, K. E. Meyer, and O. Pust, Dynamic mode decomposition and proper orthogonal decomposition of flow in a lid-driven cylindrical cavity, in *Proceedings of the 8th International Symposium on Particle Image Velocimetry, Melbourne, Victoria, Australia, August 25-28, 2009* (2009).
- [102] Z. Bai, E. Kaiser, J. L. Proctor, J. N. Kutz, and S. L. Brunton, Dynamic mode decomposition for compressive system identification, *AIAA J.* **58**, 561 (2020).
- [103] M. R. Jovanović, P. J. Schmid, and J. W. Nichols, Sparsity-promoting dynamic mode decomposition, *Phys. Fluids* **26**, 024103 (2014).
- [104] J. L. Proctor, S. L. Brunton, and J. N. Kutz, Dynamic mode decomposition with control, *SIAM J. Appl. Dyn. Syst.* **15**, 142 (2016).
- [105] Y. Zhang, L. Liu, Y. Chen, and J. Ouyang, Characteristics of ionic wind in needle-to-ring corona discharge, *J. Electrostat.* **74**, 15 (2015).
- [106] Y. Guan, R. S. Vaddi, A. Aliseda, and I. Novosselov, Experimental and numerical investigation of electro-hydrodynamic flow in a point-to-ring corona discharge, *Phys. Rev. Fluids* **3**, 14 (2018).
- [107] Y. Guan, R. S. Vaddi, A. Aliseda, and I. Novosselov, Analytical model of electro-hydrodynamic flow in corona discharge, *Phys. Plasmas* **25**, 083507 (2018).
- [108] See Supplemental Material at <http://link.aps.org/supplemental/10.1103/PhysRevE.101.033103> for details of the numerical method, code validation, and error analysis.
- [109] N. Goodnight, CUDA/OpenGL fluid simulation, NVIDIA Corporation (2007).
- [110] J. Cheng, M. Grossman, and T. McKercher, *Professional Cuda C Programming* (John Wiley & Sons, New York, NY, 2014).
- [111] D. Storti and M. Yurtoglu, *CUDA for Engineers: An Introduction to High-performance Parallel Computing* (Addison-Wesley Professional, Boston, MA, 2015).
- [112] <https://github.com/gyf135>
- [113] J. A. Domaradzki and R. W. Metcalfe, Direct numerical simulations of the effects of shear on turbulent Rayleigh-Bénard convection, *J. Fluid Mech.* **193**, 499 (1988).